A Parameter Identification Method Based on Reduced-Order Observer for SPMSM With Deadbeat Predictive Current Control

Xiao Chen, Shuo Zhang, Mingwei Zhao, Yue Zhao, Ying Zhou, Shulin Wang, and Xudong Zhang

***Abstract*—Deadbeat predictive current control (DPCC) is widely adopted in surface-mounted permanent magnet synchronous motors due to its superior control performance. However, DPCC heavily relies on the accuracy of the motor mathematical model, which means that parameter mismatches can induce current errors and pulsations. To enhance the parameter robustness of DPCC, this article proposes an online parameter identification method based on a reduced-order observer. First, sensitivity analysis of stator resistance, stator inductance, and rotor flux linkage is conducted to investigate current errors caused by individual parameter mismatches. Subsequently, stator inductance is estimated based on voltage equations, with recursive least squares. A reduced-order state observer is then employed to estimate rotor flux linkage, accompanied by stability analysis of the observer. Finally, the current control performance and parameter identification effectiveness of DPCC with the proposed method are analyzed by simulations and comparative experiments. It is verified that the proposed method effectively suppresses steady-state current errors and harmonic components induced by parameter mismatches.**

***Index Terms*—Parameter identification, recursive least squares (RLS), reduced-order observer, surface-mounted permanent magnet synchronous motor (SPMSM).**

I. Introduction

SURFACE-MOUNTED permanent magnet synchronous motors (SPMSMs) are widely adopted in industrial applications such as automobiles, elevators, and so on due to their good reliability, high power density, high efficiency, and precise control capability [1], [2].

A. Literature Review

Control strategies for PMSM can be categorized into two primary frameworks: field-oriented control (FOC) and direct torque control. Among these, FOC has gained widespread adoption due to its superior control precision and minimized torque pulsations [3]. Building upon FOC architecture, various current control methodologies have been developed, including hysteresis current control [4], proportional-integral control [5], and model predictive control. In contrast to these two methods, model predictive current control exhibits excellent steady-state and dynamic performance with enhanced control bandwidth [6], [7]. Particularly, deadbeat predictive current control (DPCC)—characterized by its straightforward implementation principle, computational simplicity, and exceptional transient response—has attracted substantial research attention and found extensive industrial applications [8], [9].

As a model-based control strategy, DPCC is susceptible to the accuracy of motor parameters. During practical motor operation, critical parameters, including rotor flux linkage, stator inductance, and stator resistance, may deviate from their nominal values due to temperature variations and magnetic saturation effects. Such mismatches exacerbate multiple operational challenges: current harmonic distortion, current tracking deviations, torque pulsations, and efficiency deterioration [10], [11].

To enhance the parameter robustness of DPCC, methods such as disturbance observation and parameter identification have been proposed. The disturbance observer-based method operates by continuously observing and compensating disturbance quantities induced by parameter mismatch, thereby indirectly addressing model inaccuracies. In contrast, parameter identification techniques directly estimate actual motor parameters, categorized into offline and online identification [12]. Since motor parameters vary dynamically during operation, online parameter identification has emerged as a predominant research focus. Online parameter identification can be categorized into numerical methods, observer-based methods, and AI-based methods [13].

Numerical methods perform iterative parameter identification based on motor mathematical models and measured data, including low-pass filters, recursive least squares (RLS), extended Kalman filtering (EKF), and model reference adaptive system (MRAS). Xiao and Griffo [14] construct a rotor flux linkage identification formula using the q-axis current equation and voltage measurements, and employ low-pass filters to eliminate noise in flux linkage calculations. RLS and EKF are essentially filtering algorithms. RLS has been widely

Received 3 June 2025; revised 18 August 2025 and 9 October 2025; accepted 4 November 2025. Date of publication 6 November 2025; date of current version 19 January 2026. Recommended for publication by Associate Editor X. Zhang. *(Corresponding author: Shuo Zhang.)*

Xiao Chen, Shuo Zhang, Mingwei Zhao, Ying Zhou, Shulin Wang, and Xudong Zhang are with the School of Mechanical Engineering and Collaborative Innovation Center of Electric Vehicles in Beijing, Beijing Institute of Technology, Beijing 100081, China (e-mail: 3120240344@bit.edu.cn; shuozhang@bit.edu.cn; 3120215226@bit.edu.cn; 7520240241@bit.edu.cn; 3120225241@bit.edu.cn; Xudong.zhang@bit.edu.cn).

Yue Zhao is with the Locomotive & Car Research Institute, China Academy of Railway Sciences Corporation Ltd., Beijing 100081, China (e-mail: z003038@zemt.cn).

Color versions of one or more figures in this article are available at https://doi.org/10.1109/TPEL.2025.3630056.

Digital Object Identifier 10.1109/TPEL.2025.3630056

applied to various motor parameter identifications due to its implementation simplicity: Zhang et al. [15], [16] and Zhou et al. [17] employ RLS to identify stator inductance, rotor flux linkage, and third-harmonic rotor flux linkage respectively; Feng et al. [18] derive permanent magnet flux linkage and cross-saturation inductance using polynomial-based flux models with least squares identification; Liu et al. [19] achieve decoupling of resistance and inductance through electromagnetic torque and reluctance torque, followed by RLS-based identification. EKF offers high identification accuracy but is computationally intensive. Zhou et al. [20] decouple stator inductance and rotor flux linkage based on current prediction error models and implemented EKF-based identification. Wang et al. [21] compensate rank deficiency via incremental current prediction error models and performs full-parameter identification combined with MRAS.

Unlike disturbance observers, certain observers, such as adaptive observers (AOs) and sliding-mode observers (SMOs), are employed to directly identify the electromagnetic and mechanical parameters of electric motors. [22] employs an adaptive interconnected observer to estimate stator inductance, resistance, and rotor position. [23] proposes an AO augmented with a high-frequency signal injection technique for sensorless control. AOs offer real-time parameter tuning and robustness to slow parameter variations, but suffer from slower convergence and sensitivity to measurement noise. [24] proposes a reduced-order position observer with stator-resistance adaptation for motion-sensorless PMSM drives. The reduced-order observer significantly reduces computational burden by decreasing the dimensionality of state variables, but it is unsuitable for parameter identification tasks with severe coupling effects. [25] and [26] employ the second-order terminal SMO to estimate mechanical parameters of PMSM. SMOs provide fast convergence and strong robustness against disturbances but exhibit inherent chattering effects. Some researchers combine different types of observers to leverage their respective advantages. An integrated observer comprising an extended sliding mode observer and a Luenberger observer is implemented to identify mechanical parameters [27].

AI-based methods have gradually gained widespread attention. However, these methods exhibit high computational complexity and demanding hardware requirements. Xie et al. [28] and Yang et al. [29] employ the particle swarm optimization algorithm and the superior raccoon optimization algorithm respectively to identify motor parameters.

If the rank of the PMSM model is less than the number of parameters to be identified, rank deficiency occurs, preventing estimated values from converging to correct results. Liu and Du [30] and Wang et al. [31] resolve this by injecting high-frequency current to increase the model rank while simultaneously achieving identification of four parameters. While effectively resolving rank deficiency, these methods introduce additional high-frequency harmonics or increase algorithmic complexity. An alternative strategy reduces the number of identifiable parameters. Zhang and Wang [32] neglect the stator resistance with negligible influence and substitute stator inductance for rotor flux linkage.

B. Motivation and Innovation

The conventional DPCC method relies on precise motor mathematical models. Consequently, its control performance degrades under parameter mismatch conditions. Specifically, mismatches in stator inductance and rotor flux linkage have particularly pronounced impacts. The primary motivation of this article is to propose an easily implementable online identification method for stator inductance and rotor flux linkage in order to enhance parameter robustness of DPCC. The principal innovations of the proposed method are summarized as follows.

1) Based on the physical characteristics of stator inductance and rotor flux linkage, an RLS algorithm with forgetting factor and an adaptive reduced-order observer are integrated and employed for the identification of these two parameters, ensuring ease of implementation and satisfactory identification performance.
2) To eliminate cross-coupling effects from rotor flux linkage mismatch during stator inductance identification, a stator inductance estimation model is formulated based on the d-axis voltage equation.
3) The rotor flux linkage is extended as a state variable in the motor system, estimated through a reduced-order state observer. A self-adaptive feedback gain that adjusts with motor speed is employed to balance estimation stability and dynamic convergence speed.

C. Paper Organization

This article is organized as follows. Section II introduces the principles of DPCC for SPMSM, followed by parameter sensitivity analysis. Section III details the online identification methodology for stator inductance and rotor flux linkage using RLS and a reduced-order observer. Section IV presents comparative simulation studies between conventional DPCC and the DPCC with the proposed parameter identification method under various operating conditions, demonstrating enhanced current control performance. Section V conducts experiment studies under corresponding operational scenarios to further verify the practical effectiveness of the proposed method. Section VI concludes this article with key findings and contributions.

II. Parameter Sensitivity Analysis in DPCC of SPMSM

A. Deadbeat Predictive Current Control

DPCC has emerged as a promising strategy for SPMSM due to its rapid dynamic response and inherent compatibility with digital control system. The structural diagram of the DPCC method is illustrated in Fig. 1.

The dynamic model of PMSM is derived from a two-phase winding system in the rotor rotating reference frame, consisting of the direct axis (d-axis) and quadrature axis (q-axis) [33]. For SPMSM, the d-axis and q-axis stator inductances can be considered equal, i.e., $L_s = L_d = L_q$. The d-q axis stator voltage equations for an SPMSM are presented as follows:

$$\begin{cases} u_d = R_s i_d + L_s \frac{di_d}{dt} - \omega_e L_s i_q \\ u_q = R_s i_q + L_s \frac{di_q}{dt} + \omega_e L_s i_d + \omega_e \psi_f \end{cases} \tag{1}$$

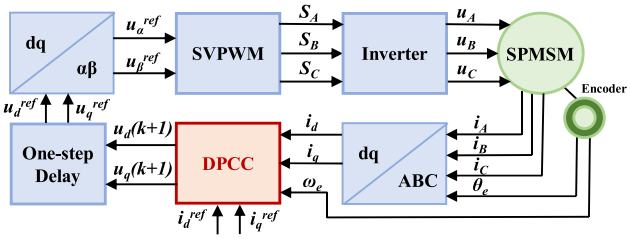

Fig. 1. Structural diagram of the DPCC method.

where u_d and u_q represent the d-axis and q-axis stator voltages; i_d and i_q denote the d-axis and q-axis stator currents; ω_e is the electrical angular velocity; R_s is the stator resistance; L_s is the stator inductance, and ψ_f is the rotor flux linkage.

By rearranging (1), the continuous-time state-space representation of the SPMSM can be derived as follows:

$$\dot{x} = Ax + Bu + C \tag{2}$$

with

$$x = \begin{pmatrix} i_d & i_q \end{pmatrix}^T, u = \begin{pmatrix} u_d & u_q \end{pmatrix}^T$$
$$A = \begin{pmatrix} -\frac{R_s}{L_s} & \omega_e \\ -\omega_e & -\frac{R_s}{L_s} \end{pmatrix}, B = \begin{pmatrix} \frac{1}{L_s} \\ \frac{1}{L_s} \end{pmatrix}, C = \begin{pmatrix} 0 \\ -\frac{\omega_e}{L_s}\psi_f \end{pmatrix}.$$

In digital control systems, it is necessary to convert the continuous-time motor model into a discrete-time counterpart. In addition, the issue of delay compensation arises: the voltages calculated in the (k)th sampling period cannot be applied to the motor until the (k+1)th period, thereby requiring the currents at the (k+1)th instant for voltage computation [34]. To address these issues, DPCC employs the first-order Euler formula to discretize (2) and (1), yielding the current prediction equation and voltage computation equation as follows:

$$\begin{cases} {i_d}^{\text{pre}}(k+1) = \left(1 - \frac{R_s T_s}{L_s}\right) i_d(k) + T_s \omega_e i_q(k) \\ \quad + \frac{T_s}{L_s} u_d(k) \\ {i_q}^{\text{pre}}(k+1) = \left(1 - \frac{R_s T_s}{L_s}\right) i_q(k) - T_s \omega_e i_d(k) \\ \quad - \frac{T_s}{L_s}\omega_e \psi_f + \frac{T_s}{L_s} u_q(k) \end{cases} \tag{3}$$

$$\begin{cases} u_d(k+1) = \left(R_s - \frac{L_s}{T_s}\right) {i_d}^{\text{pre}}(k+1) + \frac{L_s}{T_s} {i_d}^{\text{ref}} \\ \quad - \omega_e L_s {i_q}^{\text{pre}}(k+1) \\ u_q(k+1) = \left(R_s - \frac{L_s}{T_s}\right) {i_q}^{\text{pre}}(k+1) + \frac{L_s}{T_s} {i_q}^{\text{ref}} \\ \quad + \omega_e L_s {i_d}^{\text{pre}}(k+1) + \omega_e \psi_f \end{cases} \tag{4}$$

where ${i_d}^{\text{pre}}(k+1)$ and ${i_q}^{\text{pre}}(k+1)$ represent the predicted d-axis and q-axis currents at the (k+1)th sampling instant; $i_d(k)$ and $i_q(k)$ represent the d-axis and q-axis currents at the (k)th sampling instant; ${i_d}^{\text{ref}}$ and ${i_q}^{\text{ref}}$ represent the d-axis and q-axis reference currents; $u_d(k)$, $u_q(k)$, $u_d(k+1)$, and $u_q(k+1)$, respectively, denote the voltages applied to the d-axis and q-axis at the (k)th and (k+1)th sampling instants; T_s is the sampling time.

As demonstrated in (3), DPCC predicts the stator currents at the (k+1)th instant during the (k)th sampling period. These predicted currents are then incorporated into (4) to calculate the stator voltages at the (k+1)th instant, thereby achieving delay compensation.

B. Parameter Sensitivity Analysis

DPCC relies on accurate motor model and parameters. However, during motor operation, the actual values of critical parameters may deviate from their nominal values, leading to adverse effects on the performance of the control system. Therefore, analyzing the parameter sensitivity of DPCC is of critical importance.

This section will respectively discuss the prediction current error and voltage error caused by the mismatch of stator resistance R_s, stator inductance L_s and rotor flux linkage ψ_f. Suppose the actual parameter values R_{s0}, L_{s0}, and ψ_{f0} deviate from the nominal values R_s, L_s, and ψ_f employed in the control algorithm by ΔR_s, ΔL_s, and $\Delta\psi_f$.

When only stator resistance mismatch exists, substituting $R_s = R_{s0} + \Delta R_s$ and R_{s0} into (3) and (4) respectively, followed by computing their differences, yields the predicted current and voltage errors as

$$\begin{cases} \Delta {i_d}^{\text{pre}}(k+1) = -\frac{T_s \Delta R_s}{L_s} i_d(k) \\ \Delta {i_q}^{\text{pre}}(k+1) = -\frac{T_s \Delta R_s}{L_s} i_q(k) \end{cases} \tag{5}$$

$$\begin{cases} \Delta u_d(k+1) = \Delta R_s \begin{bmatrix} {i_d}^{\text{pre}}(k+1) + \left(1 - \frac{T_s R_{s0}}{L_s}\right) i_d(k) \\ + \omega_e T_s i_q(k) \end{bmatrix} \\ \Delta u_q(k+1) = \Delta R_s \begin{bmatrix} {i_q}^{\text{pre}}(k+1) + \left(1 - \frac{T_s R_{s0}}{L_s}\right) i_q(k) \\ - \omega_e T_s i_d(k) \end{bmatrix} \end{cases}. \tag{6}$$

When only stator inductance mismatch exists, substituting $L_s = L_{s0} + \Delta L_s$ and L_{s0} into (3) and (4) respectively, yields the predicted current error voltage errors as

$$\begin{cases} \Delta {i_d}^{\text{pre}}(k+1) = \frac{T_s \Delta L_s}{L_{s0}(L_{s0}+\Delta L_s)} \left[R_{s0} i_d(k) - u_d(k)\right] \\ \Delta {i_q}^{\text{pre}}(k+1) = \frac{T_s \Delta L_s}{L_{s0}(L_{s0}+\Delta L_s)} \begin{bmatrix} R_{s0} i_q(k) + \omega_e \psi_{f0} \\ - u_q(k) \end{bmatrix} \end{cases} \tag{7}$$

$$\begin{cases} \Delta u_d(k+1) = \frac{\Delta L_s}{T_s}\left({i_d}^{\text{ref}} - {i_d}^{\text{pre}}\right) + \left(R_s - \frac{L_{s0}+\Delta L_s}{T_s}\right) \Delta {i_d}^{\text{pre}} \\ \quad - \omega_e \left(L_{s0} \Delta {i_q}^{\text{pre}} + \Delta L_s {i_q}^{\text{pre}}\right) \\ \Delta u_q(k+1) = \frac{\Delta L_s}{T_s}\left({i_q}^{\text{ref}} - {i_q}^{\text{pre}}\right) + \left(R_s - \frac{L_{s0}+\Delta L_s}{T_s}\right) \Delta {i_q}^{\text{pre}} \\ \quad + \omega_e \left(L_{s0} \Delta {i_d}^{\text{pre}} + \Delta L_s {i_d}^{\text{pre}}\right) \end{cases}. \tag{8}$$

When only rotor flux linkage mismatch exists, substituting $\psi_f = \psi_{f0} + \Delta\psi_f$ and ψ_{f0} into (3) and (4) respectively, yields the predicted current error voltage errors as

$$\begin{cases} \Delta {i_d}^{\text{pre}}(k+1) = 0 \\ \Delta {i_q}^{\text{pre}}(k+1) = -\frac{T_s}{L_s}\omega_e \Delta\psi_f \end{cases} \tag{9}$$

$$\begin{cases} \Delta u_d(k+1) = {\omega_e}^2 T_s \Delta\psi_f \\ \Delta u_q(k+1) = \left(2 - \frac{T_s R_{s0}}{L_{s0}}\right) \omega_e \Delta\psi_f \end{cases}. \tag{10}$$

As indicated by (5)–(10), during steady-state motor operation, mismatches in stator resistance R_s or rotor flux linkage ψ_f will induce constant errors in the predicted currents and voltages, resulting in steady-state deviations between the actual currents and their reference values. Conversely, a mismatch in stator inductance L_s introduces oscillatory errors in the predicted currents and voltages, causing the d- and q-axis currents to oscillate around their reference values. Furthermore, the errors caused by stator resistance mismatch are significantly smaller than those arising from rotor flux linkage and stator inductance mismatches. Due to their relatively minor impact, stator resistance mismatches can be neglected to a certain extent. Therefore, this article focuses primarily on the online identification of stator inductance L_s and rotor flux linkage ψ_f.

III. Identification of Motor Parameter

The rotor flux linkage is a field quantity generated by permanent magnet and exhibits slow-varying behavior, which can be extended as a state variable. A reduced-order observer is utilized to estimate rotor flux linkage, offering both implementation simplicity and reliable performance. Since the observer is constructed based on the motor model and depends on accurate stator inductance parameter, it is necessary to perform independent identification of the stator inductance prior to estimating the rotor flux linkage.

The stator inductance is directly proportional to the permeability of the magnetic core. Influenced by the magnetic saturation level of the core, the stator inductance can undergo rapid shifts under dynamic conditions with abrupt current changes, such as severe load transients, thus requiring an identification algorithm with fast convergence. To address this, the RLS algorithm combined with the physical motor model is employed for stator inductance identification.

A. Stator Inductance Identification by RLS

RLS algorithm is an adaptive filtering technique that recursively updates parameter estimates by minimizing the sum of exponentially weighted squared errors, making it particularly suitable for real-time identification of motor parameters. Assuming that the unknown parameter x to be identified satisfies the following identification model:

$$Y = A \cdot x \tag{11}$$

where Y represents the output vector and A represents the input matrix, both of which are utilized to determine the parameter x.

When sufficient input-output data are available, it is necessary to employ the least squares method to obtain the least squares estimates of x, thereby mitigating the effects of model noise and measurement noise

$$\hat{x} = \left(A^T A\right)^{-1} A^T Y. \tag{12}$$

In real-time parameter identification, where both the output vector Y and the input matrix A undergo continuous updates, it is imperative to employ the RLS algorithm for real-time updates of the estimated parameter $x\hat{}$

$$\hat{x}_k = \hat{x}_{k-1} + \left({A_k}^T A_k\right)^{-1} {a_k}^T \left(y_k - a_k \hat{x}_{k-1}\right) \tag{13}$$

where $x\hat{}_k$ and $x\hat{}_{k\text{-}1}$ represent the parameter estimates at the (k)th and (k-1)th sampling instants; a_k and y_k correspond to the newly acquired input and output data at the (k)th sampling instant; $A_k = (a_0; a_1; \ldots; a_{k\text{-}1}; a_k)$ denotes the input matrix composed of all input vectors from the initial sampling instant up to the (k)th sampling instant.

Based on (13), the covariance matrix is defined as $P_k = (A_k{}^T A_k)^{-1}$. To circumvent matrix inversion operations, P_k is typically transformed into an equivalent form using the Sherman-Morrison Formula

$$P_k = \left(I - \frac{P_{k-1} a_k {a_k}^T}{1 + {a_k}^T P_{k-1} a_k}\right) P_{k-1} \tag{14}$$

where $P_{k\text{-}1} = (A_{k\text{-}1}{}^T A_{k\text{-}1})^{-1}$ represents the covariance matrix of the historical input data.

According to (13) and (14), RLS can update the parameter estimate at each sampling period based on $P_{k\text{-}1}$, a_k, and y_k. However, if an excessive amount of historical data is accumulated, RLS may fail to track changes in the stator inductance rapidly. Therefore, a forgetting factor λ is employed to weight the historical data, by replacing $P_{k\text{-}1}$ with $P_{k\text{-}1}/\lambda$. In addition, the gain vector is introduced as $K_k = P_k {a_k}^T$. Consequently, the recursive formula is given below

$$\begin{cases} \hat{x}_k = \hat{x}_{k-1} + K_k \left(y_k - {a_k}^T \hat{x}_{k-1}\right) \\ K_k = \frac{P_{k-1} a_k}{\lambda + {a_k}^T P_{k-1} a_k} \\ P_k = \frac{1}{\lambda}\left(I - K_k {a_k}^T\right) P_{k-1} \end{cases}. \tag{15}$$

As indicated by (1), the q-axis voltage equation simultaneously contains both parameters to be identified—stator inductance L_s and rotor flux linkage ψ_f—whereas the d-axis voltage equation contains only the stator inductance L_s. Therefore, this section will employ the RLS algorithm based on the d-axis equation to identify L_s.

Since RLS is based on a linear model, it is significant to reformulate the d-axis voltage equation into the form shown in (11). Considering that SPMSMs operate under the $i_d = 0$ control strategy, both i_d and its derivative di_d/dt can be approximated as zero. The stator inductance identification model based on the d-axis voltage equation can be expressed as

$$y_k = a_k \cdot x \tag{16}$$

with

$$\begin{cases} x = L_s \\ y_k = u_d(k) \\ a_k = -\omega_e i_q(k) \end{cases}$$

where u_d (k) is the voltage applied to the $d$axis at the (k)th sampling instant; i_q (k) is the stator current on the q-axis at the (k)th sampling instant.

In practical applications, the value of the forgetting factor λ influences both the convergence speed and accuracy of RLS. A smaller forgetting factor enables RLS to track variations in the stator inductance more rapidly, but simultaneously increases its sensitivity to noise. To mitigate the impact of noise while maintaining satisfactory convergence speed, this paper sets $\lambda = 0.995$.

B. Rotor Flux Linkage Identification With Reduced-Order Observer

To address the adverse impact of rotor flux linkage mismatch, a Luenberger observer is employed for online identification of the rotor flux linkage. To ensure that the Luenberger observer can effectively estimate the rotor flux linkage, it is essential to reformulate the state-space representation presented in (2) accordingly. First of all, the rotor flux linkage is extended to serve as the third state variable and the representation is discretized by using first-order differences

$$\begin{cases} x(k) = Gx(k-1) + Hu(k-1) \\ y(k-1) = Cx(k-1) \end{cases} \tag{17}$$

with

$$x(k) = \begin{pmatrix} \psi_f(k) & i_d(k) & i_q(k) \end{pmatrix}^T$$
$$x(k-1) = \begin{pmatrix} \psi_f(k-1) & i_d(k-1) & i_q(k-1) \end{pmatrix}^T$$
$$u(k-1) = \begin{pmatrix} u_d(k-1) & u_q(k-1) \end{pmatrix}^T$$
$$G = \begin{pmatrix} 1 & 0 & 0 \\ 0 & 1-\frac{T_sR_s}{L_s} & T_s\omega_e \\ -\frac{T_s\omega_e}{L_s} & -T_s\omega_e & 1-\frac{T_sR_s}{L_s} \end{pmatrix}$$
$$H = \begin{pmatrix} 0 & 0 \\ \frac{T_s}{L_s} & 0 \\ 0 & \frac{T_s}{L_s} \end{pmatrix}$$
$$C = \begin{pmatrix} 0 & 1 & 0 \\ 0 & 0 & 1 \end{pmatrix}$$

where i_d(*k*-1) and i_q(*k*-1) respectively represent the stator currents on the *d*-axis and *q*-axis at the (*k*-1)th sampling instants; u_d(*k*-1) and u_q(*k*-1) are the voltages applied to the *d*-axis and *q*-axis at the (*k*-1)th sampling instant; ψ_f(*k*-1) and ψ_f(*k*) are the rotor flux linkages at the (*k*-1)th and (*k*)th sampling instants.

The traditional Luenberger observer has the same dimension as the system, making it a full-dimensional observer. However, the state variables i_d and i_q can be directly measured by current sensors, while the remaining state variable, rotor flux linkage ψ_f, can be estimated using a one-dimensional reduced-order observer. The design of a reduced-order observer can be divided into the following three steps.

1) Decompose the system's state into two components, $x_1 = \psi_f$ and $x_2 = (i_d\ i_q)^T$, based on detectability. Here, x_1 requires reconstruction, while x_2 can be directly acquired from the measurable output y. The system structure after transformation and decomposition is illustrated in Fig. 2, where the subsystem Σ_1 enclosed by the dashed box is the one to be reconstructed. Consequently, the state-space representation of the system will take the following form:

$$\begin{pmatrix} @x_1(k) \\ x_2(k) \end{pmatrix} = \begin{pmatrix} G_{11} & G_{12} \\ G_{21} & G_{22} \end{pmatrix} \begin{pmatrix} x_1(k-1) \\ x_2(k-1) \end{pmatrix}$$

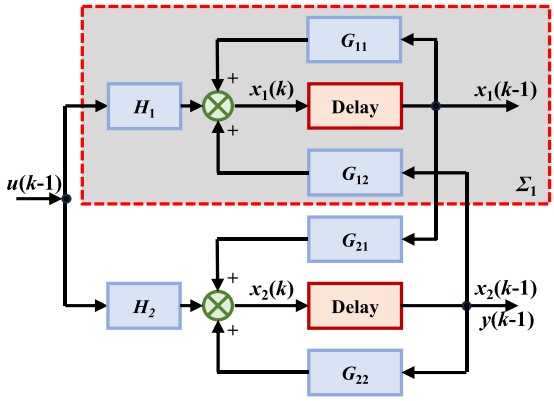

Fig. 2. Structural diagram of the system decomposed by detectability.

$$+ \begin{pmatrix} H_1 \\ H_2 \end{pmatrix} u(k-1)$$
$$y(k-1) = \begin{pmatrix} 0 & I \end{pmatrix} \begin{pmatrix} x_1(k-1) \\ x_2(k-1) \end{pmatrix} = x_2(k-1) \tag{18}$$

with

$$G_{11} = 1,\ G_{12} = \begin{pmatrix} 0 & 0 \end{pmatrix}$$
$$G_{21} = \begin{pmatrix} 0 \\ -\frac{T_s\omega_e}{L_s} \end{pmatrix},\ G_{22} = \begin{pmatrix} 1-\frac{T_sR_s}{L_s} & T_s\omega_e \\ -T_s\omega_e & 1-\frac{T_sR_s}{L_s} \end{pmatrix}$$
$$H_1 = \begin{pmatrix} 0 & 0 \end{pmatrix},\ H_2 = \begin{pmatrix} \frac{T_s}{L_s} & 0 \\ 0 & \frac{T_s}{L_s} \end{pmatrix}$$
$$y(k-1) = \begin{pmatrix} i_d(k-1) \\ i_q(k-1) \end{pmatrix},\ u(k-1) = \begin{pmatrix} u_d(k-1) \\ u_q(k-1) \end{pmatrix}.$$

1) From (18), the state-space representation of the subsystem Σ_1 can be reconstructed as follows:

$$\begin{cases} x_1(k) = G_{11}x_1(k-1) + M(k-1) \\ M(k-1) = G_{12}x_2(k-1) + H_1u(k-1) \\ z(k-1) = G_{21}x_1(k-1) = x_2(k) - G_{22}x_2(k-1) \\ \quad - H_2u(k-1) \end{cases} \tag{19}$$

where *M*(*k*-1) and *z*(*k*-1) represent the known input and output of the subsystem Σ_1 at the (*k*-1)th sampling instant.

1) In subsystem Σ_1, to verify that the state vector x_1 can be reconstructed from the output *M* and input *z*, it is necessary to analyze the observability of this subsystem. From (19), the state matrix of Σ_1 is G_{11}, the output matrix is G_{21}, and the number of state variables is $n = 1$. Thus, the observability matrix *N* of this discrete-time system is

$$N = \begin{pmatrix} G_{21} \\ G_{21}G_{11} \\ \vdots \\ G_{21}{G_{11}}^{n-1} \end{pmatrix} = G_{21} = \begin{pmatrix} 0 \\ -\frac{T_s\omega_e}{L_s} \end{pmatrix}. \tag{20}$$

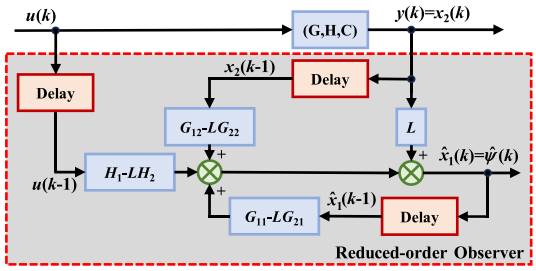

Fig. 3. Structural diagram of the reduced-order observer.

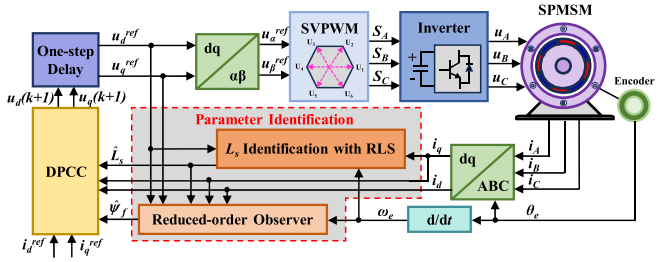

Fig. 4. Control block diagram of DPCC with the proposed parameter identification method.

From (20), it is evident that the rank of the observability matrix N is 1 when the motor speed $\omega_e \neq 0$, proving that subsystem Σ_1 is fully observable.

The traditional Luenberger observer is an asymptotic state observer. Building upon the open-loop observer framework, it incorporates a feedback correction channel that utilizes the output y to rectify the state estimation error. By adopting the aforementioned design methodology, the equation of the reduced-order observer can be derived as follows:

$$\hat{x}_1(k) = (G_{11} - LG_{21})\hat{x}_1(k-1) + M(k-1) + Lz(k-1) \tag{21}$$

where $\hat{x}_1(k\text{-}1)$ and $\hat{x}_1(k)$ represent the estimates of the state $x_1 = \psi_f$ at the (k-1)th and (k)th0 sampling instants, respectively; L is the feedback matrix of the observer to be designed.

By substituting (19) into (21), the identification equation for the rotor flux linkage is derived as follows:

$$\begin{aligned}\hat{\psi}_f(k) = {} & (G_{11} - LG_{21})\hat{\psi}_f(k-1) + (G_{12} - LG_{22})y(k-1) \\ & + (H_1 - LH_2)u(k-1) + Ly(k)\end{aligned} \tag{22}$$

where $\widehat{\Psi}_f(k-1)$ and $\widehat{\Psi}_f(k-1)$ are the identification results of the rotor flux linkage at the (k-1)th and (k)th sampling instants, respectively.

The structural diagram of the reduced-order observer is illustrated in Fig. 3. According to (1), the rotor flux linkage exclusively influences the q-axis current and remains independent of the d-axis current. Therefore, feedback correction of the estimated rotor flux linkage only requires utilizing the sensor-detected q-axis current. Set $L = (0\ l_2)$.

The parameter identification method proposed in this article utilizes the measured dq-axis currents and rotor electrical angular speed, along with the calculated dq-axis voltage commands as inputs to accomplish parameter identification. The method consists of two sequential stages: First, an independent and decoupled identification of stator inductance is performed based on the d-axis voltage equation using the RLS algorithm. Subsequently, the updated stator inductance estimate is employed in the reduced-order observer for rotor flux linkage identification. The DPCC algorithm utilizes these estimated parameter values for current prediction and voltage calculation. Fig. 4 shows the control block diagram of the DPCC algorithm incorporating the proposed parameter identification method.

C. Stability Analysis for the Reduced-Order Observer

To analyze the impact of the feedback matrix on the stability of the reduced-order observer, the state estimation error is introduced as follows:

$$e(k) = x_1(k) - \hat{x}_1(k). \tag{23}$$

Subsequently substituting (19) and (21) into (23), the state estimation error equation is derived as

$$\begin{aligned}e(k) &= G_{11}x_1(k-1) + M(k-1) - (G_{11} - LG_{21})\hat{x}_1(k-1) \\ &\quad - M(k-1) - Lz(k-1) \\ &= G_{11}x_1(k-1) - (G_{11} - LG_{21})\hat{x}_1(k-1) - LG_{21}x_1(k-1) \\ &= (G_{11} - LG_{21})e(k-1).\end{aligned} \tag{24}$$

From (24), the stability of the observer depends on the eigenvalues of the matrix G_{11}–LG_{21}. If the magnitudes of all eigenvalues of G_{11}–LG_{21} are less than 1 (i.e., lie within the unit circle), the estimation error $e(k)$ will asymptotically converge to zero over time, and the observer is thereby stabilized.

To ensure the estimated rotor flux linkage asymptotically converges to its true value, the feedback matrix $L = (0\ l_2)$ must satisfy the following inequality:

$$\left|\lambda\left(G_{11} - LG_{21}\right)\right| = \left|1 + \frac{T_s\omega_e}{L_s}l_2\right| < 1 \Rightarrow -\frac{2L_s}{T_s\omega_e} < l_2 < 0 \tag{25}$$

where $\lambda(G_{11}$–$LG_{21})$ is the eigenvalue of the matrix G_{11}–LG_{21}.

As shown in (25), the poles of matrix G_{11}–LG_{21} can be arbitrarily assigned by selecting the feedback gain l_2, thereby influencing the convergence of observation errors. Simultaneously, the poles of G_{11}–LG_{21} are also affected by the motor speed ω_e.

When the poles are close to the origin (i.e., $|\lambda(G_{11}\text{-}LG_{21})| \to 0$), the observer achieves faster convergence but may amplify noise or high-frequency disturbances. Conversely, when the poles approach the unit circle boundary (i.e., $|\lambda(G_{11}\text{-}LG_{21})| \to 1$), the observer exhibits slower convergence but stronger robustness against noise and disturbances.

If fixed feedback gain l_2 is selected, the observer's convergence speed becomes slower at low speeds and gradually improves as the speed increases, albeit at the cost of reduced disturbance rejection. To ensure consistent convergence performance across different speeds (i.e., to maintain uniform pole placement), the proposed reduced-order observer adaptively

TABLE I
PARAMETERS OF SPMSM

Parameter	Description	Value
P_N	Rated power(kW)	1
T_{max}	Max Torque(Nm)	10
P	Number of pole pairs	4
R_{s0}	Stator resistance(Ω)	0.365
L_{s0}	Stator inductance(mH)	1.225
ψ_{f0}	Rotor flux linkage(Wb)	0.1667

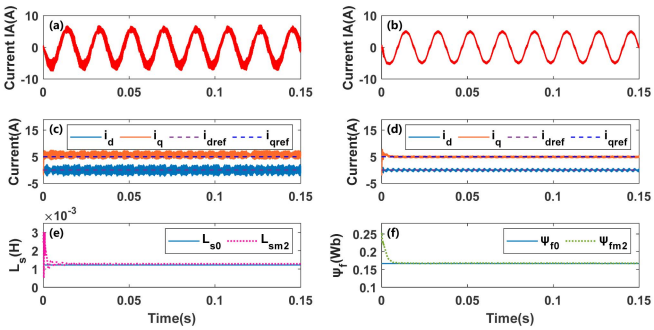

Fig. 5. Simulation results under 2-fold L_s mismatch and 1.5-fold ψ_f mismatch at 800 r/min and 5 N·m. (a) and (c) Method 1. (b) and (d) Method 2. (e) and (f) Identification results of method 2.

adjusts the feedback gain l_2 based on the motor speed ω_e, as expressed in the following equation:

$$l_2 = -k\frac{L_s}{T_s\omega_e}, k \in (0, 2) \tag{26}$$

where k is a tunable gain for achieving different pole configurations. Based on simulation and experimental results, this article ultimately sets $k = 0.0274$.

IV. SIMULATION STUDY

To preliminarily verify the effectiveness of DPCC with the proposed parameter identification method, an SPMSM simulation model is established on the MATLAB/Simulink platform for simulation study. The relevant parameters of the SPMSM are shown in Table I. The inverter's switching frequency is 20 kHz, the controller's sampling time is 50 μs and the dead time is set to 2.5 μs. This section will present the current control performance of both methods, where method 1 is the conventional DPCC and the method 2 is the DPCC with the proposed parameter identification method. The parameter identification results of method 2 will also be demonstrated.

Fig. 5 demonstrates the current control performance of both methods under steady-state motor operation with a two-fold mismatch in stator inductance and rotor flux linkage, along with the parameter identification results of method 2. The motor operates at a speed of 800 r/min and a torque of 5 N·m. As shown in Fig. 5, the parameter mismatch causes significant current disturbances in method 1, with a steady-state error in the q-axis current. In contrast, the parameter estimates of method 2 converge to the vicinity of the true values within a short period, enabling the currents to accurately track the reference values and significantly reducing disturbances.

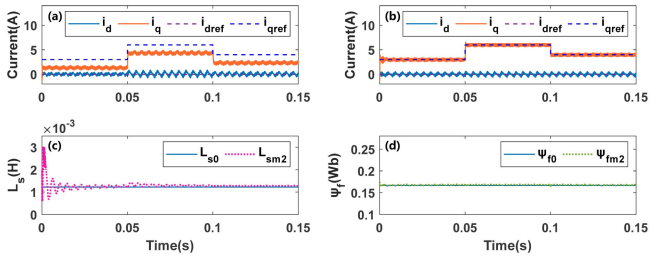

Fig. 6. Simulation results under 0.5-fold L_s mismatch at 600 r/min and 3-6-4 N·m. (a) Method 1. (b) Method 2. (c) and (d) Identification results of method 2.

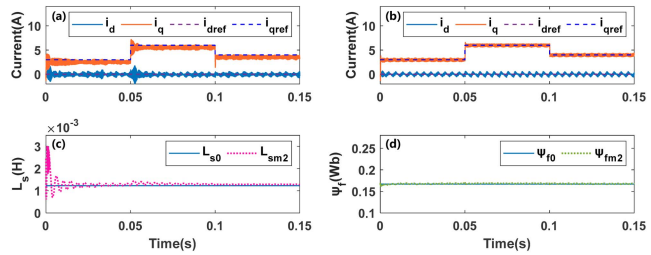

Fig. 7. Simulation results under 2-fold L_s mismatch at 600 r/min and 3-6-4 N·m. (a) Method 1. (b) Method 2. (c) and (d) Identification results of method 2.

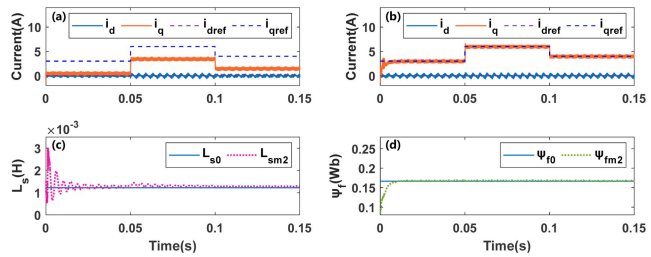

Fig. 8. Simulation results under 0.5-fold ψ_f mismatch at 600 r/min and 3-6-4 N·m. (a) Method 1. (b) Method 2. (c) and (d) Identification results of method 2.

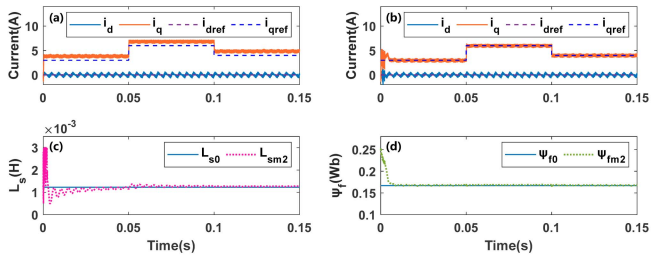

Fig. 9. Simulation results under 1.5-fold ψ_f mismatch at 600 r/min and 3-6-4 N·m. (a) Method 1. (b) Method 2. (c) and (d) Identification results of method 2.

Figs. 6–9 present the d-q axis current control performance of both methods under different parameter mismatch conditions during step changes in motor torque, along with the parameter identification results of method 2. The motor operates at a speed of 600 r/min, with the torque undergoing step changes from 3 to 6 to 4 N·m. As evidenced by these figures, method 2 effectively handles various parameter mismatch scenarios, enabling accurate tracking of reference values for the d-q axis currents. Notably, the parameter identification results remain

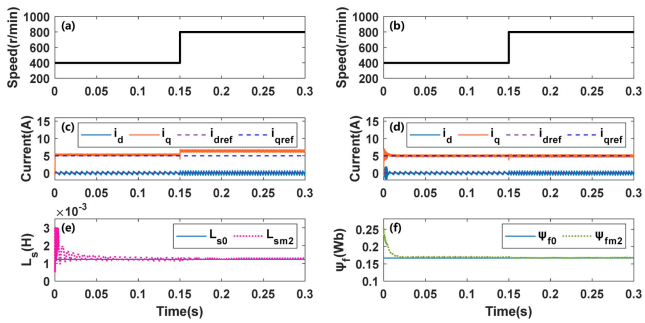

Fig. 10. Simulation results under 1.5-fold ψ_f mismatch at 400–800 r/min and 5 N·m. (a) and (c) Method 1. (b) and (d) Method 2. (e) and (f) Identification results of method 2.

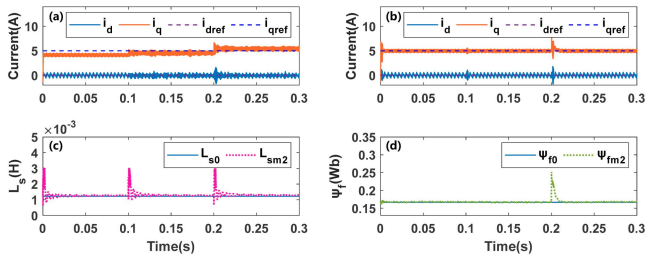

Fig. 11. Simulation results under parameter step at 600 r/min and 5 N·m. (a) Method 1. (b) Method 2. (c) and (d) Identification results of method 2.

unaffected by step changes in motor torque, demonstrating strong robustness.

As indicated in (9) and (10), the error caused by rotor flux linkage mismatch is speed-dependent. Fig. 10 demonstrates the currents and parameter identification results of both methods under a 1.5-fold rotor flux linkage mismatch condition during step changes in motor speed. The motor speed steps from 400 to 800 r/min, with the torque maintained at 5 N·m. The results reveal that method 1 exhibits increased steady-state current tracking error during the speed step, whereas the currents of method 2 remain unaffected by the speed transient.

Fig. 11 presents the currents and parameter identification results of both methods under step changes in stator inductance and rotor flux linkage, respectively. The motor operates at a speed of 600 r/min with a torque of 5 N·m. In contrast to method 1, method 2 rapidly identifies accurate parameters within a short duration, suppresses errors induced by abrupt parameter mismatch, and ensures precise tracking of current reference values.

V. Experimental Study

To further validate the feasibility of the proposed method, experimental studies are conducted on the experimental platform shown in Fig. 12. The current control performance of method 1 and method 2 is compared under different operating conditions. In addition, this section compares three parameter identification methods: the proposed method (method 2), the decoupled parameter identification method with Kalman filtering (KF) [20] (method 3), and the parameter identification method with only reduced-order observer (method 4). The digital signal processor employed in the control board is TMS320F28377d, while the

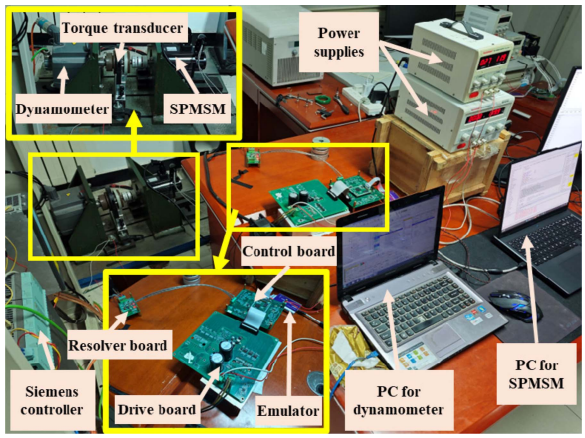

Fig. 12. Experiment platform.

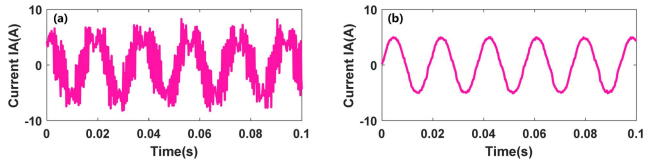

Fig. 13. Experiment results of phase-A current under 2-fold L_s mismatch and 1.5-fold ψ_f mismatch at 800 r/min and 5 N·m. (a) Method 1. (b) Method 2.

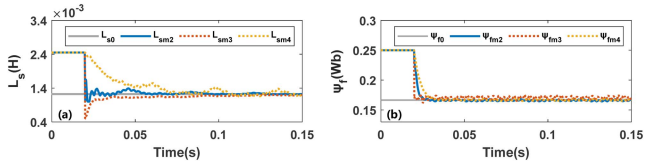

Fig. 14. Parameter identification results under 2-fold L_s mismatch and 1.5-fold ψ_f mismatch at 800 r/min and 5 N·m. (a) Stator inductance. (b) Rotor flux linkage.

decoder chip integrated in the resolver board is AD2S1200, and the power module utilized in the drive board is FNB43060T2. The inverter's switching frequency is 20 kHz, the controller's sampling time is 50 μs and the dead time is set to 2.5 μs. The dc supply voltage is set to 120 V.

During steady-state motor operation, the current control performance of methods 1 and 2 is comparatively evaluated under parameter mismatch conditions (2-fold stator inductance mismatch and 1.5-fold rotor flux linkage mismatch). Fig. 13 demonstrates the phase-A current waveforms of both methods at a motor speed of 800 r/min with 5 N·m torque. Method 1 exhibits a total harmonic distortion (THD) of 76.34% in its phase-A current, whereas method 2 achieves a significantly reduced THD of 4.88%, indicating that the proposed method can effectively mitigates current harmonic components induced by parameter mismatches.

Fig. 14 shows the parameter identification results of methods 2, 3, and 4 at 800 r/min and 5 N·m. The RLS algorithm used in method 2 achieved convergence of the stator inductance estimate within 720 sampling periods (36 ms), with an error within $\pm 3\%$. Meanwhile, the reduced-order observer achieved convergence of the rotor flux linkage estimate within 176 sampling periods

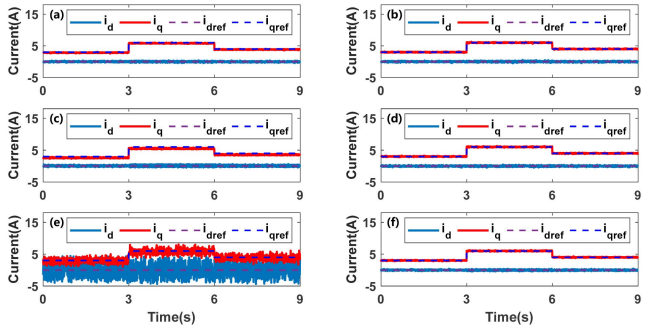

Fig. 15. Experiment results of d-q-axis currents at 600 r/min and 3-6-4 N·m. (a) and (b) Methods 1 and 2 under no parameter mismatch. (c) and (d) Methods 1 and 2 under 0.5-fold L_s mismatch. (e) and (f) Methods 1 and 2 under 2-fold L_s mismatch.

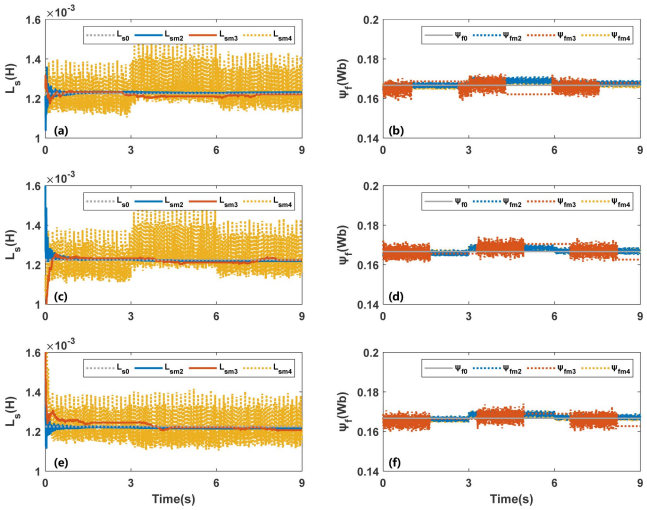

Fig. 16. Parameter identification results at 600 r/min and 3-6-4 N·m. (a) and (b) Stator inductance and rotor flux linkage under no parameter mismatch. (c) and (d) Stator inductance and rotor flux linkage under 0.5-fold L_s mismatch. (e) and (f) Stator inductance and rotor flux linkage under 2-fold L_s mismatch.

(8.8 ms), with an error within ±2%. Compared with method 3, method 2 exhibits faster identification speed for stator inductance and slightly slower but more accurate identification of rotor flux linkage. In comparison with method 4, method 2 demonstrates superior performance in both identification speed and accuracy, proving that the combined use of RLS and the reduced-order observer better matches the characteristics of the two parameters.

During torque step changes of the motor, the current performance of methods 1 and 2 under parameter mismatch conditions is presented in Figs. 15 and 17. The motor operates at 600 r/min while undergoing stepped torque variations from 3 to 6 to 4 N·m. Figs. 16 and 18 display the parameter identification results of methods 2, 3, and 4 under these operating conditions. Method 2 demonstrates accurate identification of actual parameter values across various mismatch scenarios, effectively suppressing steady-state current errors and harmonic components. The stator inductance estimation error of method 4 is relatively large, which demonstrates the necessity of using RLS instead of the reduced-order observer for stator inductance identification. Compared

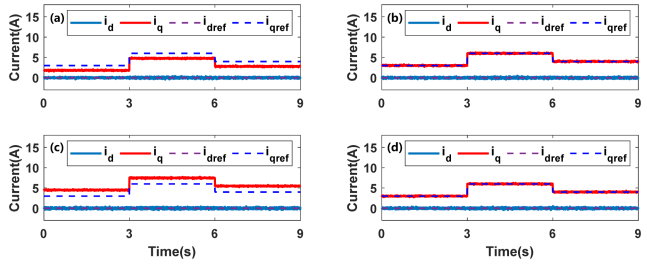

Fig. 17. Experiment results of d-q-axis currents at 600 r/min and 3-6-4 N·m. (a) and (b) Methods 1 and 2 under 0.7-fold ψ_f mismatch. (c) and (d) Methods 1 and 2 under 1.5-fold ψ_f mismatch.

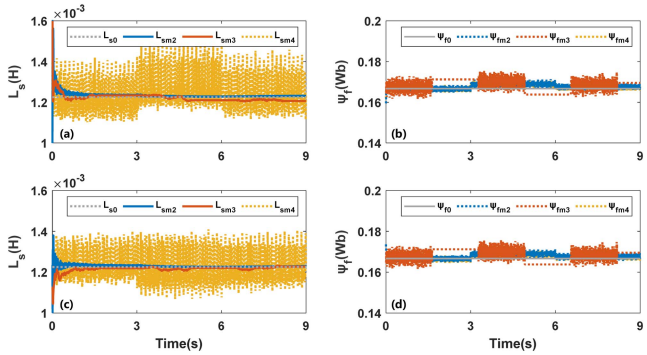

Fig. 18. Parameter identification results at 600 r/min and 3-6-4 N·m. (a) and (b) Stator inductance and rotor flux linkage under 0.7-fold ψ_f mismatch. (c) and (d) Stator inductance and rotor flux linkage under 1.5-fold ψ_f mismatch.

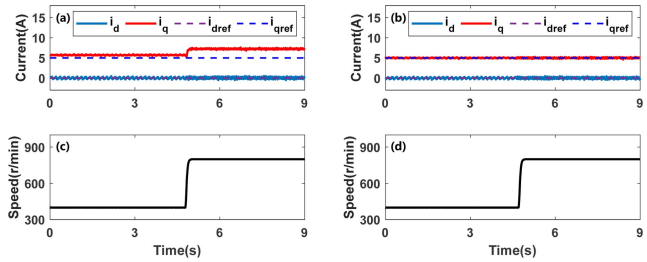

Fig. 19. Experiment results of d-q-axis currents at 400—800 r/min and 5 N·m. (a) and (c) Method 1 under 1.5-fold ψ_f mismatch. (b) and (d) Method 2 under 1.5-fold ψ_f mismatch.

with method 3, method 2 exhibits better stability during torque step changes.

During step changes in motor speed, the current control performance of methods 1 and 2 under 1.5-fold rotor flux linkage mismatch are illustrated in Fig. 19. The motor speed undergoes a step change from 400 to 800 r/min while maintaining a constant torque of 5 N·m. The results demonstrate that rotor flux linkage mismatch induces varying degrees of steady-state current errors at different motor speeds, which are effectively eliminated by method 2.

Fig. 20 displays the parameter identification results of methods 2, 3, and 4. Compared with method 3, method 2 demonstrates better stability in stator inductance identification under speed step conditions. Although both method 2 and method 3 exhibit jumps in rotor flux linkage estimation during speed steps, method 2's advantage lies in its faster re-convergence of the rotor

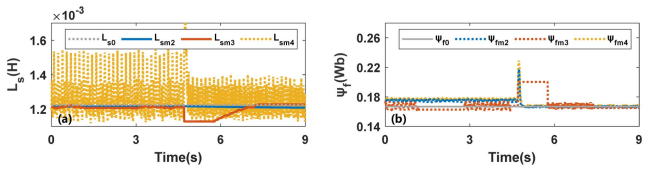

Fig. 20. Parameter identification results at 400–800r/min and 5 N·m. (a) Stator inductance under 1.5-fold ψ_f mismatch. (b) Rotor flux linkage under 1.5-fold ψ_f mismatch.

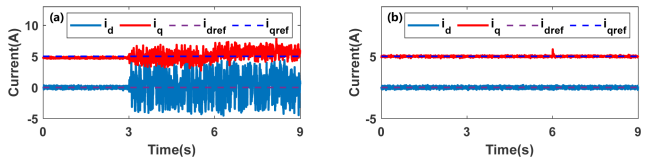

Fig. 21. Experiment results of *d*-*q*-axis currents at 600 r/min and 5 N·m under stator inductance step at 3 s and rotor flux linkage step at 6 s. (a) Method 1. (b) Method 2.

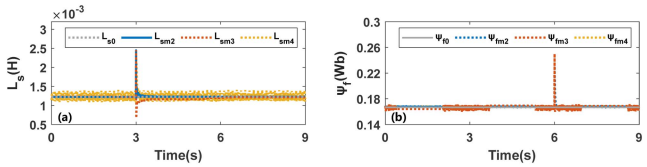

Fig. 22. Parameter identification results of *d*-*q*-axis currents at 600 r/min and 5 N·m under stator inductance step at 3 s and rotor flux linkage step at 6 s. (a) Stator inductance. (b) Rotor flux linkage.

TABLE II
PROGRAM EXECUTION TIME COMPARISON

Method	Execution time
1: Conventional DPCC	5.86μs
2: DPCC with proposed method	12.44μs
3: DPCC with KF	18.28μs
4: DPCC with only reduced-order observer	10.10μs

flux estimation. The rotor flux identification results of method 4 are comparable to those of method 2, but its stator inductance identification performance is significantly inferior.

To investigate the current control performance of methods 1 and 2 under abrupt parameter mismatch, step changes in stator inductance and rotor flux linkage are introduced at different time instants, with experiment results presented in Fig. 21. The motor operates at 600 r/min with a constant torque of 5 N·m. Fig. 22 presents the parameter identification results of methods 2, 3, and 4. As evidenced by the results, method 2 maintains essentially unaffected *d*-*q*-axis currents during abrupt parameter mismatch through rapid parameter identification.

The execution times of methods 1–4 are presented in Table II. Compared with method 1, method 2 requires additional computational time due to its parameter identification method. However, this compromise is justified by its significantly improved current control performance under parameter mismatch conditions. When benchmarked against method 3, method 2 demonstrates superior computational efficiency with shorter execution time, highlighting its advantage in algorithmic complexity. Relative to method 4, method 2 achieves remarkable improvements in both identification speed and accuracy while introducing only marginal additional computational overhead. In conclusion, method 2 effectively enhances the control system's robustness against parameter mismatches while fully satisfying real-time operation requirements.

VI. CONCLUSION

In this article, to enhance the parameter robustness of DPCC in SPMSM applications, an online parameter identification method is proposed. The conclusions are summarized as follows.

1) Parameter sensitivity analysis and experiment results reveal that for conventional DPCC, stator inductance mismatch induces increased current disturbances; rotor flux linkage mismatch causes steady-state tracking errors; stator resistance mismatch generates comparatively negligible errors, avoiding rank-deficiency problems.
2) RLS and a reduced-order observer are respectively employed for identifying stator inductance and rotor flux linkage. The inductance identification formula, derived from the *d*-axis voltage equation, remains immune to flux linkage mismatch interference. Stability analysis and speed-adaptive gain adjustment of the reduced-order observer balances convergence speed and robustness regardless of operating conditions.
3) Simulation and experiment results demonstrate that the proposed method achieves rapid and accurate motor parameter identification across various operating conditions, significantly enhancing both steady-state and dynamic performance of DPCC under parameter mismatch scenarios.

REFERENCES

[1] B. Xia et al., "Encoderless deadbeat predictive current control for SPMSM drives with online parameter identification," *IEEE Trans. Transp. Electrific.*, vol. 11, no. 1, pp. 761–773, Feb. 2025.
[2] H. Lin, S. Niu, Z. Xue, and S. Wang, "A simplified virtual-vector-based model predictive control technique with a control factor for three-phase SPMSM drives," *IEEE Trans. Power Electron.*, vol. 38, no. 6, pp. 7546–7557, Jun. 2023.
[3] J. Li, Y. Sun, H. Dan, X. Li, F. Zhou, and M. Su, "SPMSM adaptive control with guaranteed dynamic response under parameter mismatch," *IEEE Trans. Power Electron.*, vol. 39, no. 12, pp. 16471–16481, Dec. 2024.
[4] S. Jayaprakasan, S. Ashok, and R. Ramchand, "Current error space vector based hysteresis controller for VSI fed PMSM drive," *IEEE Trans. Power Electron.*, vol. 35, no. 10, pp. 10690–10699, Oct. 2020.
[5] J. Wen, X. Yuan, S. Niu, and W. L. Chan, "A robust complex vector PI current controller with deadbeat response for PMSM drives," *IEEE Trans. Ind. Electron.*, vol. 72, no. 5, pp. 4671–4681, May 2025.
[6] C.-K. Lin, T.-H. Liu, J - Yu, L.-C. Fu, and C.-F. Hsiao, "Model-free predictive current control for interior permanent-magnet synchronous motor drives based on current difference detection technique," *IEEE Trans. Ind. Electron.*, vol. 61, no. 2, pp. 667–681, Feb. 2014.
[7] H. Liu, W. Lin, Z. Liu, C. Buccella, and C. Cecati, "Model predictive current control with model-aid extended State observer compensation for PMSM drive," *IEEE Trans. Power Electron.*, vol. 38, no. 3, pp. 3152–3162, Mar. 2023.
[8] F. Wang, W. Kong, and R. Qu, "Model parameter self-correcting deadbeat predictive current control for SPMSM drives," *IEEE Trans. Ind. Electron.*, vol. 72, no. 3, pp. 2357–2368, Mar. 2025.

[9] L. Wang, J. Zhao, X. Yang, Z. Zheng, X. Zhang, and L. Wang, "Robust deadbeat predictive current regulation for permanent magnet synchronous linear motor drivers with parallel parameter disturbance and load observer," *IEEE Trans. Power Electron.*, vol. 37, no. 7, pp. 7834–7845, Jul. 2022.

[10] M. Tian, B. Wang, Y. Yu, Q. Dong, and D. Xu, "Static-errorless deadbeat predictive current control for PMSM current harmonics suppression based on vector resonant controller," *IEEE Trans. Power Electron.*, vol. 38, no. 4, pp. 4585–4595, Apr. 2023.

[11] Z. Hao, Y. Yang, K. Shao, and Y. Liu, "Switching active disturbance rejection based deadbeat predictive current control for permanent magnet synchronous motors," *IEEE Trans. Power Electron.*, vol. 38, no. 11, pp. 13920–13932, Nov. 2023.

[12] C. Lian, F. Xiao, J. Liu, and S. Gao, "Parameter and VSI nonlinearity hybrid estimation for PMSM drives based on recursive least square," *IEEE Trans. Transp. Electrific.*, vol. 9, no. 2, pp. 2195–2206, Jun. 2023.

[13] M. S. Rafaq and J.-W. Jung, "A comprehensive review of State-of-the-art parameter estimation techniques for permanent magnet synchronous motors in wide speed range," *IEEE Trans. Ind. Inform.*, vol. 16, no. 7, pp. 4747–4758, Jul. 2020.

[14] S. Xiao and A. Griffo, "PWM-based flux linkage and rotor temperature estimations for permanent magnet synchronous machines," *IEEE Trans. Power Electron.*, vol. 35, no. 6, pp. 6061–6069, Jun. 2020.

[15] J. Zhang, F. Peng, Y. Huang, Y. Yao, and Z. Zhu, "Online inductance identification using PWM current ripple for position sensorless drive of high-speed surface-mounted permanent magnet synchronous machines," *IEEE Trans. Ind. Electron.*, vol. 69, no. 12, pp. 12426–12436, Dec. 2022.

[16] H. Zhang, T. Fan, L. Meng, J. Guo, and X. Wen, "Polynomial estimation of flux linkage for predictive current control in PMSM," *IEEE J. Emerg. Sel. Topics Power Electron.*, vol. 10, no. 5, pp. 6112–6122, Oct. 2022.

[17] Y. Zhou, S. Zhang, X. Cui, C. Zhang, and X. Li, "An accurate torque output method for open-end winding permanent magnet synchronous motors drives," *IEEE Trans. Energy Convers.*, vol. 36, no. 4, pp. 3470–3480, Dec. 2021.

[18] G. Feng, C. Lai, X. Tan, W. Peng, and N. C. Kar, "Multi-parameter estimation of PMSM using differential model with core loss compensation," *IEEE Trans. Transp. Electrific.*, vol. 8, no. 1, pp. 1105–1115, Mar. 2022.

[19] Z. Liu, Y. Han, G. Feng, and N. C. Kar, "Efficient nonlinear multi-parameter decoupled estimation of PMSM drives based on multi-State voltage and torque measurements," *IEEE Trans. Energy Convers.*, vol. 38, no. 1, pp. 321–331, Mar. 2023.

[20] Y. Zhou, S. Zhang, C. Zhang, X. Li, X. Li, and X. Yuan, "Current prediction error based parameter identification method for SPMSM with deadbeat predictive Current control," *IEEE Trans. Energy Convers.*, vol. 36, no. 3, pp. 1700–1710, Sep. 2021.

[21] L. Wang, S. Zhang, C. Zhang, and Y. Zhou, "An improved deadbeat predictive current control based on parameter identification for PMSM," *IEEE Trans. Transp. Electrific.*, vol. 10, no. 2, pp. 2740–2753, Jun. 2024.

[22] M. A. Hamida, J. De Leon, A. Glumineau, and R. Boisliveau, "An adaptive interconnected observer for sensorless control of PM synchronous motors with online parameter identification," *IEEE Trans. Ind. Electron.*, vol. 60, no. 2, pp. 739–748, Feb. 2013.

[23] A. Piippo, M. Hinkkanen, and J. Luomi, "Adaptation of motor parameters in sensorless PMSM drives," *IEEE Trans. Ind. Appl.*, vol. 45, no. 1, pp. 203–212, Jan-Feb. 2009.

[24] M. Hinkkanen, T. Tuovinen, L. Harnefors, and J. Luomi, "A combined position and stator-resistance observer for salient PMSM drives: Design and stability analysis," *IEEE Trans. Power Electron.*, vol. 27, no. 2, pp. 601–609, Feb. 2012.

[25] Y. Feng, X. Yu, and F. Han, "High-order terminal sliding-mode observer for parameter estimation of a permanent-magnet synchronous motor," *IEEE Trans. Ind. Electron.*, vol. 60, no. 10, pp. 4272–4280, Oct. 2013.

[26] D. Liang, J. Li, R. Qu, and W. Kong, "Adaptive second-order sliding-mode observer for PMSM sensorless control considering VSI nonlinearity," *IEEE Trans. Power Electron.*, vol. 33, no. 10, pp. 8994–9004, Oct. 2018.

[27] Z. Liao et al., "An integrated observer framework based mechanical parameters identification for adaptive control of permanent magnet synchronous motor," *Complex System Model. Simul.*, vol. 2, no. 4, pp. 354–367, Dec. 2022.

[28] C. Xie, S. Zhang, X. Li, Y. Zhou, and Y. Dong, "Parameter identification for SPMSM with deadbeat predictive current control using online PSO," *IEEE Trans. Transp. Electrific.*, vol. 10, no. 2, pp. 4055–4064, Jun. 2024.

[29] X. Yang, J. Zhan, Y. Shen, P. Liu, L. Guo, and Z. Zhang, "Parameter identification for SPMSM based on a superior ROA," *IEEE Trans. Power Electron.*, vol. 40, no. 6, pp. 7615–7627, Jun. 2025.

[30] X. Liu and Y. Du, "Torque control of interior permanent magnet synchronous motor based on online parameter identification using sinusoidal current injection," *IEEE Access*, vol. 10, pp. 40517–40524, 2022.

[31] Y. Wang et al., "A robust DPCC for IPMSM based on a full parameter identification method," *IEEE Trans. Ind. Electron.*, vol. 70, no. 8, pp. 7695–7705, Aug. 2023.

[32] X. Zhang and Z. Wang, "Simple robust model predictive current control for PMSM drives without flux-linkage parameter," *IEEE Trans. Ind. Electron.*, vol. 70, no. 4, pp. 3515–3524, Apr. 2023.

[33] X. Wu, H. Chen, B. Liu, T. Wu, C. Wang, and S. Huang, "Improved deadbeat predictive current control of PMSM based on a resistance adaptive position observer," *IEEE Trans. Transp. Electrific.*, vol. 10, no. 3, pp. 5215–5224, Sep. 2024.

[34] Z. Liu et al., "A modified deadbeat predictive current control for improving dynamic performance of PMSM," *IEEE Trans. Power Electron.*, vol. 37, no. 12, pp. 14173–14185, Dec. 2022.